Time-resolved and time-averaged stereo-PIV measurements of a unit-ratio cavity

Exp Fluids (2016) 57:101
DOI 10.1007/s00348-016-2186-9

RESEARCH ARTICLE

Time-resolved and time-averaged stereo-PIV measurements of a unit-ratio cavity

Marc Immer[1,2] · **Jonas Allegrini**[1,2] · **Jan Carmeliet**[1,2]

Received: 11 September 2015 / Revised: 12 May 2016 / Accepted: 13 May 2016 / Published online: 31 May 2016

Abstract An experimental setup was developed to perform wind tunnel measurements on a unit-ratio, 2D open cavity under perpendicular incident flow. The open cavity is characterized by a mixing layer at the cavity top, that divides the flow field into a boundary layer flow and a cavity flow. Instead of precisely replicating a specific type of inflow, such as a turbulent flat plate boundary layer or an atmospheric boundary layer, the setup is capable of simulating a wide range of inflow profiles. This is achieved by using triangular spires as upstream turbulence generators, which can modify the otherwise laminar inflow boundary layer to be moderately turbulent and stationary, or heavily turbulent and intermittent. Measurements were performed by means of time-resolved stereo PIV. The cavity shear layer is analyzed in detail using flow statistics, spectral analysis, and space–time plots. The ability of the setup to generate typical cavity flow cases is demonstrated for characteristic inflow boundary layers, laminar and turbulent. Each case is associated with a distinct shear layer flow phenomena, self-sustained oscillations for the former and Kelvin–Helmholtz instabilities for the latter. Additionally, large spires generate a highly turbulent wake flow, resulting in a significantly different cavity flow. Large turbulent sweep and ejection events in the wake flow suppress the typical shear layer and sporadic near wall sweep events generate coherent vortices at the upstream edge.

1 Introduction

Open cavities have the ability to exchange mass and momentum with the external flow. Under perpendicular incident flow, they are often also called *shear-driven cavities*. In a shear-driven cavity the interface is defined by a mixing layer between the cavity flow and the external boundary layer flow, in contrast to the lid-driven cavity, where the top is a closed moving surface. This shear layer is governed through complex dynamical phenomena, arising through flow instabilities that are influenced by the external flow and through feedback mechanisms between the impinging flow on the downstream edge, the cavity flow and the shear layer flow.

Shear-driven cavities have been initially researched for their relevance in aeronautics, where drag and vibrations were the primary interest, for example in panel gaps, wheel wells or weapon bays. The experimental wind tunnel research by Roshko (1955), Rossiter and Britain (1964), and Sarohia (1975) have explored the existence of resonance in the shear layer, generated through acoustic and hydrodynamic feedback. This phenomenon of *self-sustained oscillations* can occur when a shear layer impinges on a downstream obstacle, such as present in a cavity under certain conditions (Rockwell 1977; Rockwell and Naudascher 1978; Knisely and Rockwell 1982). Based on the area of research, the flow conditions for these studies are therefore usually for thin laminar or turbulent boundary layers at high Reynolds Numbers or high Mach numbers.

Electronic supplementary material The online version of this article (doi:10.1007/s00348-016-2186-9) contains supplementary material, which is available to authorized users.

✉ Marc Immer
marc.immer@gmail.com

[1] Chair of Building Physics, Institute of Technology in Architecture, ETH, Swiss Federal Institute of Technology Zurich, Zurich, Switzerland

[2] Laboratory for Multiscale Studies in Building Physics, Empa, Swiss Federal Laboratories for Materials Science and Technology, Dubendorf, Switzerland

Besides aerospace and transportation, a strong interest in the cavity geometry was also shown in atmospheric sciences, especially in the field of pollutant dispersion (e.g., Johnson et al. 1973; Nicholson 1975) and thermal modelling. (e.g., Nunez and Oke 1977). The space in between two elongated buildings can be idealized as the so called *Street Canyon*. Under perfectly perpendicular flow conditions, the cavity top is the only way the street level can exchange air, and therefore pollutant and heat, with the flow aloft. Based on wind tunnel measurements conducted by Hussain and Lee (1980) and Oke (1988) identified different flow regimes based on the aspect ratio of the cavity, that range from skimming flow for a deep canyon (high aspect ratio) to isolated roughness flow for a very wide canyon (low aspect ratio). The upstream flow for street canyon measurements is usually defined as a thick turbulent atmospheric or urban boundary layer profile. Under these conditions, the cavity shear layer shows properties of a free shear layer, such as vortex formation through a Kelvin–Helmholtz-type instability (e.g., Chang et al. 2006; Bian et al. 2010; Salizzoni et al. 2011).

In recent years, wind tunnel experiments have made significant contributions to the understanding of cavity-type shear flows. Specifically, imaging measurement techniques such as particle image velocimetry (PIV) (as conducted by, e.g., Ashcroft and Zhang 2005; Kang et al. 2008 or Haigermoser et al. 2008) in combination with analytical flow modelling (e.g., Chatellier et al. 2004) or advanced analysis tools such as modal analysis (e.g., Basley et al. 2010) or POD (e.g., Kang and Sung 2009; Kellnerová et al. 2012) showed the complexity of the shear layer, and its dependence on the upstream boundary layer.

The specific area of research that investigates a cavity-type flow, as described earlier, usually dictates the type and shape of the upstream flow profile. Therefore, wind tunnel tests often have the specific goal of investigating a flow phenomena (such as the before mentioned self-sustained oscillations or Kelvin–Helmholtz instabilities) typical to that specific type of inflow.

In this work, we describe an experimental setup for a unity aspect ratio cavity, that has the capability to subject the cavity to a wide range of turbulent inflow conditions, but still remain capable to reproduce the different known cavity flow phenomena. The wind tunnel tests were performed in the ETH/Empa atmospheric boundary layer wind tunnel. Time-averaged and time-resolved measurements were conducted by means of stereo PIV. Measurements were performed on a vertical plane parallel to the flow, imaging simultaneously the flow just upstream of the cavity (inlet boundary layer flow), the cavity flow itself and the flow downstream of the cavity.

This paper details the observations made for three cavity flow cases having different specific upstream wall bounded flows: a laminar boundary layer, a moderately turbulent boundary layer and a strongly turbulent wake flow. The laminar boundary layer is used to validate the experimental setup by a comparison of the observed flow phenomena with previously investigated cavity flows from literature. The specific moderately turbulent boundary layer is used to show that the selected type of turbulence generators upstream of the cavity results in shear layer dynamics similar to ones observed in existing literature of turbulent cavity flows. For the third flow, a specific type of a thick, strongly turbulent wake flow, no comparable measurement was found in literature.

In Sect. 2, we describe the experimental facilities, model setup and data evaluation in detail. This includes the PIV data acquisition, vector processing and uncertainty analysis. In Sect. 3, selected results of the performed measurements of the cavity flow and the shear layer are presented and compared, followed by an analysis and discussion of each case in Sect. 4.

2 Experimental setup

2.1 Experimental facility and measurement system

Measurements were conducted at the ETH/Empa atmospheric boundary layer wind tunnel, a closed circuit "Göttingen"-type boundary layer wind tunnel. The test section is closed and 10.4 m long, 1.9 m wide and 1.3 m high. The fan has a nominal power of 110 kW and is capable to generate free stream velocities from 0.5 up to 25 m/s in the test section. Flow seeding is provided by a system that generates 1 μm aerosol particles (DEHS). A stepper-motor-driven traversing system is installed in the last 2.6 m of the test section, allowing a probe to be moved within a 2.3 m × 0.3 m × 1.6 m volume with a step size of 1/100th mm. The linear positioning elements Rose+Krieger DuoLine Z 50 are used for all axes and feature a timing belt driven guide table with a repetition accuracy of 0.05 mm and a positioning accuracy of 0.1/300 mm. Induction switches allow to perform a reference drive to reliably set the origin of the traverse system. The traverse system is also used to define an absolute coordinate system in the test section, allowing for repeatable wind tunnel model placement and accurate PIV laser sheet alignment.

The principal measurement system used is a time-resolved stereoscopic PIV system from LaVision and is composed of two 12-bit CMOS cameras and a dual-cavity Nd:YLF laser with a wavelength of 527 nm and a maximum energy per pulse of 30 mJ (at 1 kHz repetition rate and a pulse duration of 150 ns). The cameras have a maximum resolution of 2016 × 2016 pixels at a recording frequency of up to 640 Hz. The 36 GB of memory allow

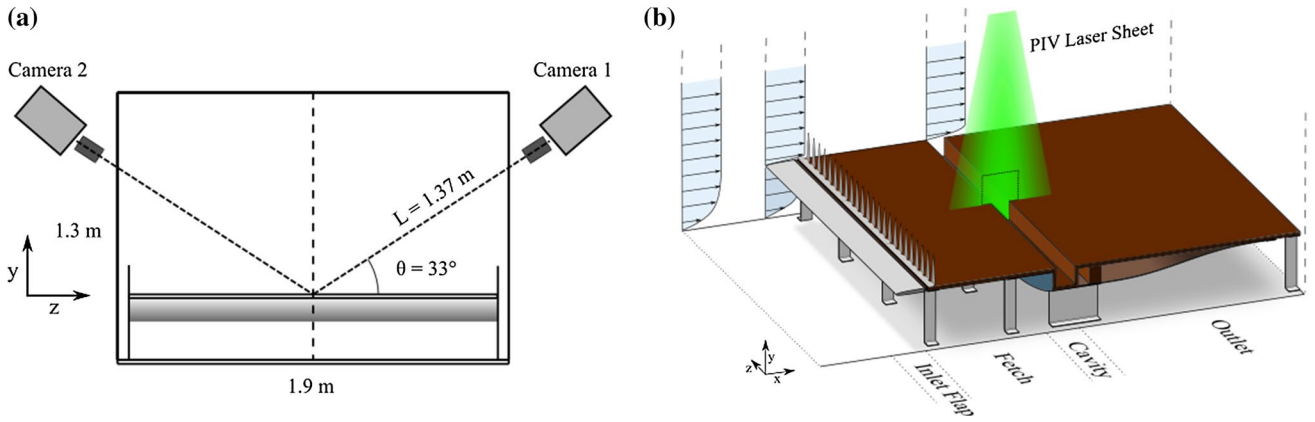

Fig. 1 **a** Wind tunnel cross section showing camera arrangement and imaging plane and **b** model of the 2D cavity with split floor showing the approach flow, laser sheet and PIV field of view (*dashed rectangle*). The cavity end caps are omitted for clarity

storage of 3155 double-frame images at full resolution. The two cameras were mounted at opposite sides of the wind tunnel test section, perpendicular to the flow and tilted down at an angle of 33° from the horizontal (Fig. 1a). The optics consisted of 135 mm F2.0 Canon objectives on a Scheimpflug mount. The light sheet, generated by a cylindrical lens above the wind tunnel, was vertically aligned with the test section center-plane.

Additionally, a Dantec hot wire system in combination with the traverse was used to sample large field turbulent flow statistics. The probe used was a Dantec 55P16 miniature single wire probe with a 1.25-mm long and 5-μm diameter platinum-plated tungsten wire. Velocity signals were acquired using the a MiniCTA single channel hot wire bridge with analog voltage output and a National Instruments NI USB-9162 A/D converter with a 10-kHz sample rate. Calibration of the probe was performed using a Dantec StreamLine Pro Automatic Calibrator to get a fifth-order calibration polynomial. A correction of the measured voltage signal was performed to account for temperature difference between the calibration temperature and the measurement temperature, prior to the conversion to velocity.

2.2 Model geometry

A split floor was installed in the downstream part of the test section, raised 31.5 cm above the wind tunnel floor (Fig. 1b). This is well above the wind tunnel boundary layer, which measures around 15 cm in height. The experimental setup is composed of four main sections: adjustable inlet flap, inlet fetch, cavity and outlet plane. The inlet flap can be deflected downwards, to prevent flow separation due to the increased blockage of the cavity model. The inlet flaps are manufactured from wire-erosion cut aluminum and have a slightly rough finish. The inlet plate, cavity and outlet plate are manufactured from phenolic coated birch plywood and have a smooth finish. The cavity height is $H_c = 100$ mm and the cavity length (width of gap between upstream and downstream edge) measures $L_c = 101.4$ mm. This results in an aspect ratio of $H_c/L_c = 0.99 \approx 1$. The complete model is 1.8 m wide, leaving a 5-cm gap on each side between the model and the wind tunnel wall. To minimize the influence of the wind tunnel walls, the cavity ends are closed, using thin 500-mm-long end caps. They extend 440 mm from the wind tunnel floor to well above the cavity, as indicated in Fig. 1a. A 200-mm-wide center section of the cavity has the horizontal surfaces (inlet, floor and outlet) equipped with flush mounted, aluminum coated front surface mirrors. The mirrors have a reflectivity above 94 %, reducing unwanted diffusion of laser light and therefore enabling near-surface measurements. This is especially important for stereo PIV, due to the angled camera setup. The model is supported by 3-mm-thin sheet metal struts. To reduce aerodynamic drag from the protruding cavity on the lower side of the model, and therefore to increase flow-through, a fairing made from Polystyrene foam and a flexible wooden plate was installed. Spires can be mounted downstream of the inlet flap, at a position $x = -608$ mm upstream of the cavity. They have a triangular shape and resemble Irwin-type spires (Irwin 1981).

2.3 Cases and PIV measurements

The cavity flow fields were measured for three different conditions. The case names defined in Table 1 will be used throughout the paper.

For the case *ThinBL*, a boundary layer was developed naturally by the inlet fetch. For the two cases *5m* and *15w*, additional turbulence was generated by spires with height 5 and 15 cm respectively. The width to height ratio of the 15 cm spire is double the value of the 5 cm spire, leading to the notion *w* for *wide* and *m* for *medium*. For the *5m* and

Table 1 Definition of measurement cases and properties of the turbulence generating spires

Case	Spire height (mm)	Spire width (mm)	Blockage (%)
ThinBL	–	–	0
5*m*	50	7.7	15.4
15*w*	150	46.2	30.8

15w spires, flow statistics of the wake flow and developing boundary layer were measured with the hot wire probe, on a vertical plane at the center line and a horizontal plane at half spire height. The spire geometry and the resulting flow fields are presented in Fig. 2.

For each case, two image sequences were recorded with the PIV system at a wind tunnel fan speed of 100 rpm. Each sequence consists of 3155 double-frame stereo images with 2016 × 2016 pixel resolution. The first sequence was recorded at 10 Hz, to provide data of the average flow field, the second sequence at 600 Hz. A separation time of 300 μs between the two frames of each double-frame image pair was found to give adequate particle shift values.

The PIV measurements are made available online (Immer 2015).

The average free stream velocity above the cavity was calculated from time-averaged measurements and was found to be $U_\infty = 3.14$ m/s for the cases *ThinBL* and *5m* and 3.36 m/s for the case *15w* with a relative SD of 0.96 %. With an air temperature of 22.3 ± 1.5 °C and standard atmospheric conditions at 440 m altitude, the Reynolds number with respect to the cavity height H_c, for the cases *ThinBL* and *5m* was calculated to be $Re = 19{,}260 \pm 175$.

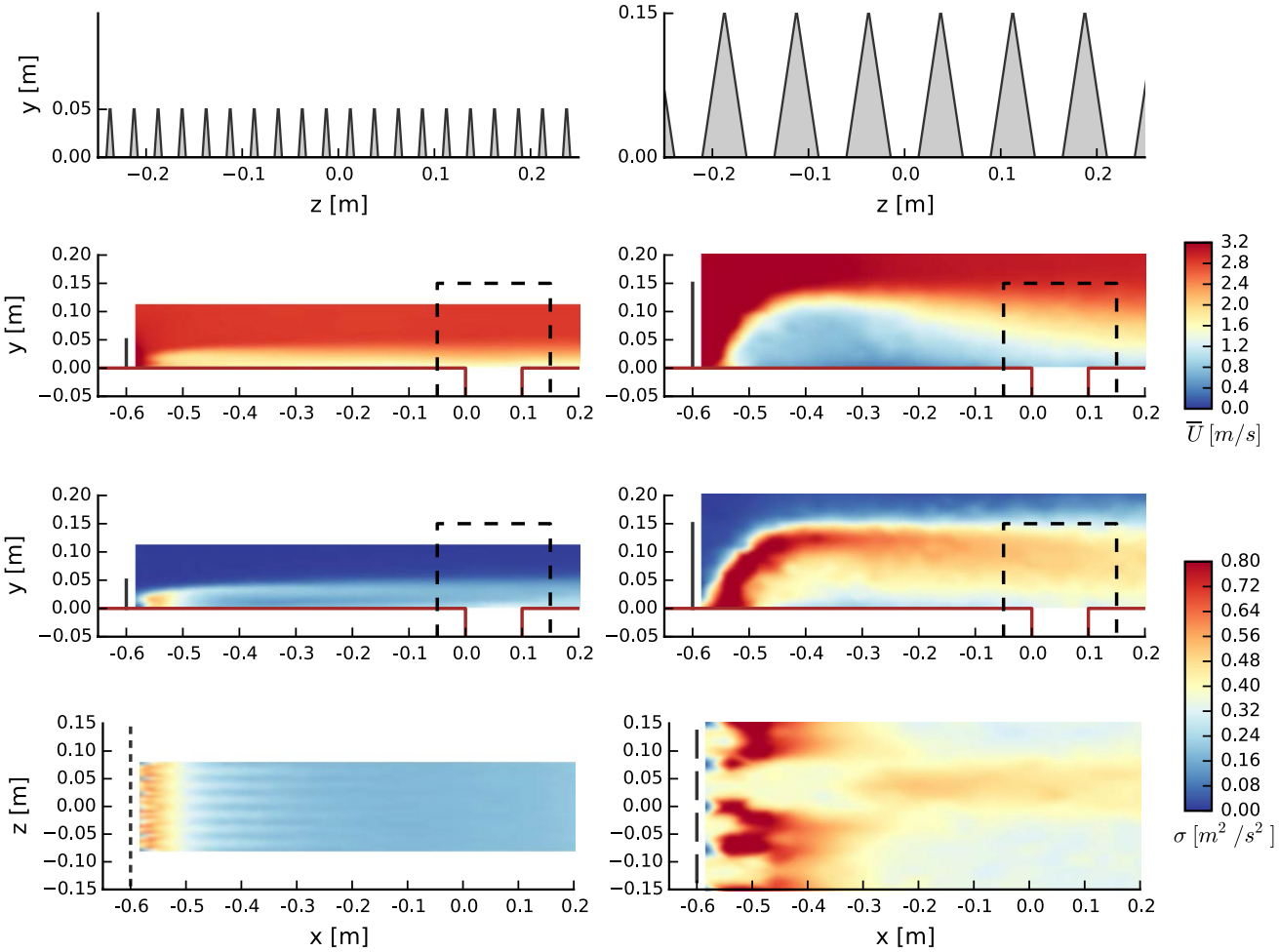

Fig. 2 Hot wire measurements for the flow fields generated by the spires *5m* (*left column*) and *15w* (*right column*). The spire geometry is shown in the *top row*, with the coordinate system on the centerline of the wind tunnel. The *second* and *third row* shows measurements on a centerline streamwise plane of the mean velocity $\overline{U}$ and SD σ respectively. The *dashed rectangle* shows the location of the PIV field of view. The *bottom row* shows σ on a *horizontal plane* at $y = 0.5\,H$

Table 2 Velocity uncertainty

Parameter	Error sources	u_c	c_i	$c_i u_c$ (m/s)
α	Calibration	6.456E−07 m/px	24,515.4 px/s	0.01582
ΔX	Image displacement	0.03 px	0.4269 m/px/s	0.01281
Δt	Image interval	3.002E−07 s	−10,466.7 m/s^2	−0.00314
	Combined			0.0206 m/s (0.66 %)

2.4 PIV vector processing and velocity post processing

Image acquisition and PIV vector processing were performed with the software DaVis 8 from LaVision GmbH. Stereo-PIV vector processing was performed on CPUs using a multi-pass approach and a final interrogation window of 24 pixels, with a 50 % window overlap. This resulted in a window size of $dx = dy = 1.574$ mm, giving 60×60 three-component velocity vectors inside the cavity. Postprocessing and data evaluation was conducted using custom written Python 2.7 code, utilizing the Numpy,[1] Scipy[2] and the in-house developed pyFlowStat[3] module.

The measured instantaneous velocity U_i with $i = (x, y, z)$ is decomposed into the mean velocity $\overline{U_i}$ and the fluctuating velocity u_i. The average flow field $\overline{U_x}, \overline{U_y}, \overline{U_z}$ and the Reynolds stress tensor $R_{ij} = \overline{u_i u_j}$ were computed from the 3155 samples in the 10 Hz time-averaged data. The averaged velocity vector for one location was only considered valid if a valid PIV vector existed at that location for all acquired samples. No additional smoothing or interpolation of gaps was performed.

Velocity gradients $\frac{\partial U_x}{\partial x}, \frac{\partial U_x}{\partial y}, \frac{\partial U_y}{\partial x}, \frac{\partial U_y}{\partial y}$ were determined using central differences at the interior and first differences at the boundaries. The out-of-plane vorticity was calculated as $\omega_z = \frac{\partial U_y}{\partial x} - \frac{\partial U_x}{\partial y}$. The vortex identification criteria Q (Hunt et al. 1988) was computed based on the two-dimensional velocity gradient tensor, since the out-of-plane gradient was not available:

$$Q^{2D} = \frac{1}{2}\left(2\frac{\partial U_x}{\partial y}\frac{\partial U_y}{\partial x} - \frac{\partial U_x}{\partial x}^2 - \frac{\partial U_y}{\partial y}^2\right). \quad (1)$$

This still allows to identify vortex cores, even if their axis of rotation is not perpendicular to the x–y plane.

Integral time scales T_x, T_y and T_z were estimated from the autocorrelation of the respective velocity component. Autocorrelations were calculated using an FFT-based procedure, and the timescale calculated subsequently by fitting an exponential function of the form $\rho(\tau) = e^{-\frac{\tau}{T}}$ with lag τ and integral time scale T. Integral length scales are derived by multiplying the time scale with the local mean velocity magnitude, implicitly assuming Taylors hypothesis of frozen turbulence.

Turbulent kinetic energy (TKE) is defined as $\mathrm{TKE} = \frac{1}{2}(\overline{u_x^2} + \overline{u_y^2} + \overline{u_z^2})$. Production of TKE is derived from the Reynolds-averaged Navier–Stokes (RANS) equation and reads in Einstein summation notation:

$$\mathcal{P}^{2D}_{\mathrm{TKE}} = -\overline{u_i u_j}\frac{\partial U_i}{\partial x_j} \quad (2)$$

with $\frac{\partial U_i}{\partial x_3} = 0$ (assuming two-dimensional flow, i.e., no out-of-plane gradients).

2.5 Measurement uncertainty

Three main areas of uncertainty have been identified that lead to errors or uncertainty: design of the experiment, PIV measurement uncertainty and statistical uncertainty.

Unwanted flow effects due to the experimental setup were reduced by careful design. Gaps and small steps between the model parts were sealed using tape, special care was taken upstream of the measurement area. End caps on the cavity reduced wall effects.

PIV uncertainty has been reduced by performing the measurements according to best practice. The laser light sheet was geometrically aligned with the wind tunnel centerline, and the camera angles set to 33° according to (LaVision 2011b). The initial camera calibration was performed prior to installing the model in the tunnel with a precision milled 20×20 cm two-level calibration plate. The camera and lens parameters were calculated by fitting a pinhole model to the calibration images. DaVis reports the SD of the fit to be 0.15 pixel. The registration error was reduced by using a stereo-PIV self-calibration procedure (Wieneke 2005). No peak locking was evident for either the cavity or the boundary layer flow, suggesting adequate particle image size (LaVision 2011a). To assess the measurement uncertainty, the sensitivity coefficients c_i for PIV equation $U = \alpha(\frac{\Delta X}{\Delta t})$ where calculated. The procedure described in ITTC (2008) was adapted. Table 2 presents the results, where α relates to the camera calibration, ΔX to the pixel displacement, Δt to the timing accuracy of the laser. ΔX was determined using the correlation statistics method (Wieneke 2014) as implemented in the Davis Software. The estimated overall PIV uncertainty is well below 1 %.

[1] http://www.numpy.org/.

[2] http://www.scipy.org/.

[3] https://github.com/ETH-BuildingPhysics/pyFlowStat.

Statistical uncertainty was assessed according to the procedure described in Nobach and Tropea (2007) assuming a normal distribution. The SD of the estimated mean for the three velocity components can be calculated by using the standard error of the mean, $\mathrm{SE}_{\overline{U_i}} = \sqrt{R_{ii}/n_{\mathrm{eff}}}$ where R_{ii} is a diagonal component of the Reynolds stress tensor, and n_{eff} the effective sample size. The effective sample size is estimated using $n_{\mathrm{eff}} = \min(n_{\mathrm{samples}}, t/2T_{xx})$ with T_{xx} being the largest integral time scale and n_{samples} the number of recorded samples. To estimate the error of the Reynolds stress, the SD of the estimator is calculated using $\sigma_{R_{ii}} = \sqrt{\mathrm{Var}(R_{ii})} = R_{ii}\sqrt{2/(n_{\mathrm{eff}} - 1)}$. The relative error therefore only depends on the sample size. With 3155 effective samples, this corresponds to 2.5 %.

3 Results

Results are presented in dimensionless form when applicable. For the length scale, the cavity height H_c is used and for the velocity scale, the free stream velocity U_∞ is used. For the cases *thinBL* and *5m*, U_∞ was measured to be 3.14 m/s. For the case *15w*, hot wire measurements showed a small increase by 7 %, due to a small influence due to the presence of the spires, resulting in $U_\infty = 3.36$ m/s. From these scales, the time scales are calculated as $\tau = H_c/U_\infty$ and result in $\tau = 0.0318$ s for the cases *thinBL* and *5m* and $\tau = 0.0298$ s s for the case *15w*.

3.1 Inlet flow and cavity flow field

Inlet flow profiles upstream of the cavity are presented in dimensionless form in Fig. 3, showing the resulting values for the normalized streamwise velocity $\overline{U}_x$, normalized TKE and normalized shear stress $\overline{u_x u_y}$. The profiles are computed from the time-averaged PIV measurements and horizontally averaged between $x/H_c = -0.4$ and $x/H_c = -0.2$. The origin of PIV coordinate system is on the upstream cavity edge (Fig. 4). The boundary layer thickness corresponds with the spire height. A clear difference in magnitude of normalized TKE characterizes the degree of turbulence for the three cases. The case *thinBL* shows virtually no normalized TKE, and the small amount visible close to the wall is accounted to reflection artifacts. The moderately turbulent case *5m* shows almost constant normalized shear stress up to $y/H_c = 0.3$. The normalized velocity profile for the case *15w* shows that this case does not represent a developed boundary layer. The CTA measurements (Fig. 2) confirm that the flow is still developing at the cavity location. Additionally, Fig. 3 also shows an estimate of the streamwise normalized integral length scale for U_x. L_{xx}/H_c is relatively constant below $y/H_c = 0.5$ and averages to 0.42 for the *15w* case, which is about 2.6 times larger compared to the case *5m* ($L_{xx}/H_c = 0.16$). The length scale is still smaller than the cavity length.

The cavity flow fields are presented in Fig.4. All three cases show a clockwise rotating main vortex within the

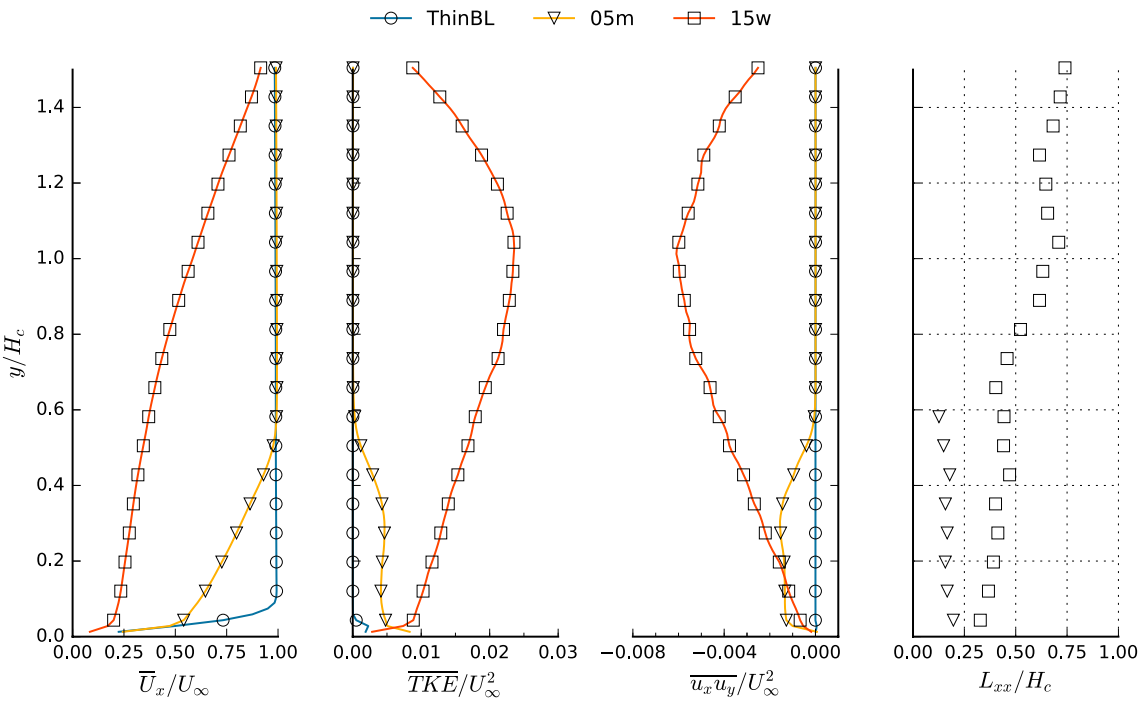

Fig. 3 Inlet flow profiles at $x/H_c = -0.3$, showing normalized mean velocity, normalized turbulent kinetic energy, normalized shear stress and normalized integral length scale. Markers are shown for every fifth datapoint

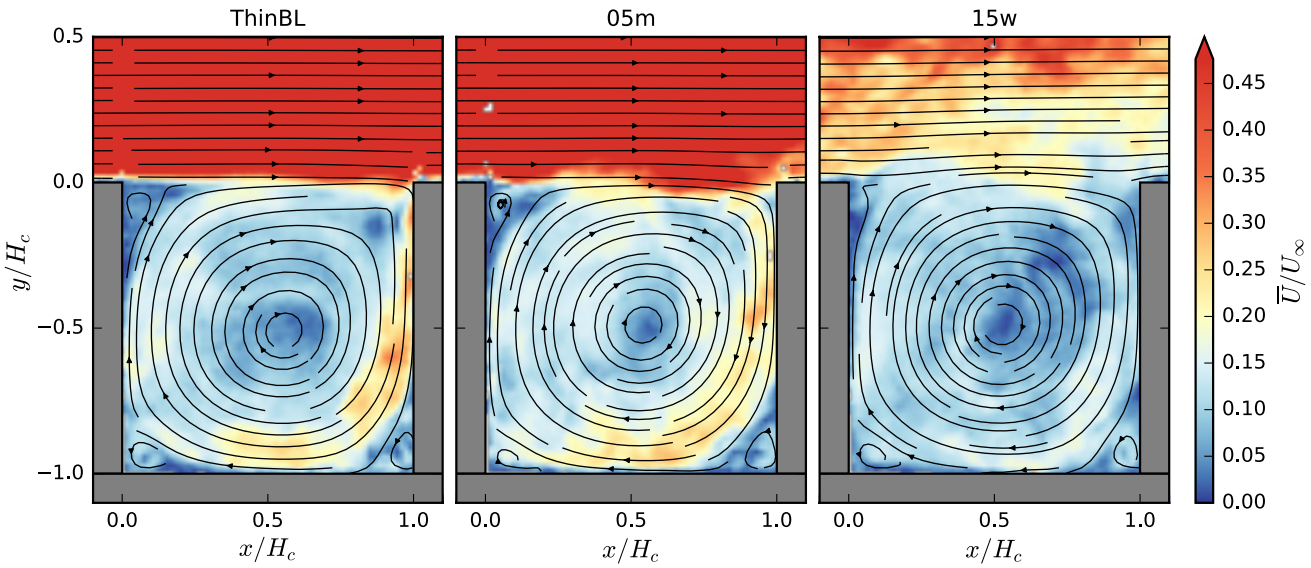

Fig. 4 Cavity flow field for the cases *ThinBL*, *5m* and *15w*, with streamlines of the mean flow field, and a snapshot of the normalized velocity magnitude (background)

cavity, and a horizontal flow above the cavity. The flow impinges on the downstream edge and is entrained into the cavity. Small corner vortices are formed in the bottom corners and in the top upstream corner. The cavity vortex is contained within the cavity by a dividing streamline, starting at the detachment point at the upstream edge and ending in the stagnation point at the downstream edge. The dividing streamline is horizontal and flat, except for the case *15w*, where the streamline slightly curves above the top. The velocity snapshot shows the structure of the turbulent flow in the cavity.

Profiles for the main flow statistics are presented on lines through the cavity center ($x_c/H_c = 0.5$, $y_c/H_c = -0.5$) in Figs. 5 and 6. The vertical profiles in Fig. 5a clearly show large gradients of normalized $\overline{U}_x$ for the cases *ThinBL* and *5m*, with an infliction point just above the cavity top. An infliction point is an necessary condition for flow instability. The location of the infliction point corresponds to the point of maximum normalized TKE and normalized shear stress. The case *15w* shows a shallow gradient and no clear peak of either normalized TKE or shear stress. The horizontal profile of normalized mean vertical velocity $\overline{U}_y$ in Fig. 5b provides information about the main cavity vortex. For both the cases *ThinBL* and *5m*, higher normalized velocities are visible on the right side wall. Consequently, due to conservation of mass, the vortex center (intersection of normalized $\overline{U}_y$ with $x/H_c = 0.5$) is offset to the right. The case *15w* shows a flatter velocity profile. From the normalized $\overline{U}_y$ it can also be seen that the average (normalized) rotation speed of the cavity vortex is the highest for the case *5m*, followed by the case *ThinBL* and *15w*. All cases show an increased peak-like normalized TKE and shear stress on the right wall. The case *ThinBL* shows a narrow and shear peak of normalized shear stress, but the lowest normalized TKE. The normalized shear stress of case *15w* shows only a small broad peak, however this case features the highest normalized TKE. The profiles of the three diagonal components of the normalized Reynolds stress tensor ($\overline{u}_x^2$, $\overline{u}_y^2$ and $\overline{u}_z^2$, being the three terms of the TKE equation) are shown in Fig. 6. Notable is the high contribution of the out-of-plane normalized Reynolds stress $\overline{u}_z^2$ to the normalized TKE on the right wall, especially for the case *15w*.

3.2 Shear layer

Besides the flow profiles, field plots of the turbulent statistics (e.g., normalized TKE and normalized shear stress) show the connection of the cavity flow to the shear layer (Fig. 7). All three cases show some normalized TKE inside the cavity, meaning that the cavity flow is always turbulent. The case *15w* shows the highest normalized TKE both inside the cavity and in the boundary layer above. Compared to the other cases, normalized TKE is also the most uniformly distributed in the cavity. The distribution of normalized TKE at the cavity top (around $y/H_c = 0$) is significantly different for each case. The case *ThinBL* shows a large amount of normalized TKE toward the downstream edge, *5m* features high normalized TKE over the entire top, linearly growing in height and the case *15w* shows a vertical gradient of normalized TKE from the cavity to the boundary layer. This gradient is quite pronounced at the upstream edge and low at the downstream edge. Especially for the cases *5m* and *15w*, TKE is also visible at the downstream cavity wall. The production of normalized TKE,

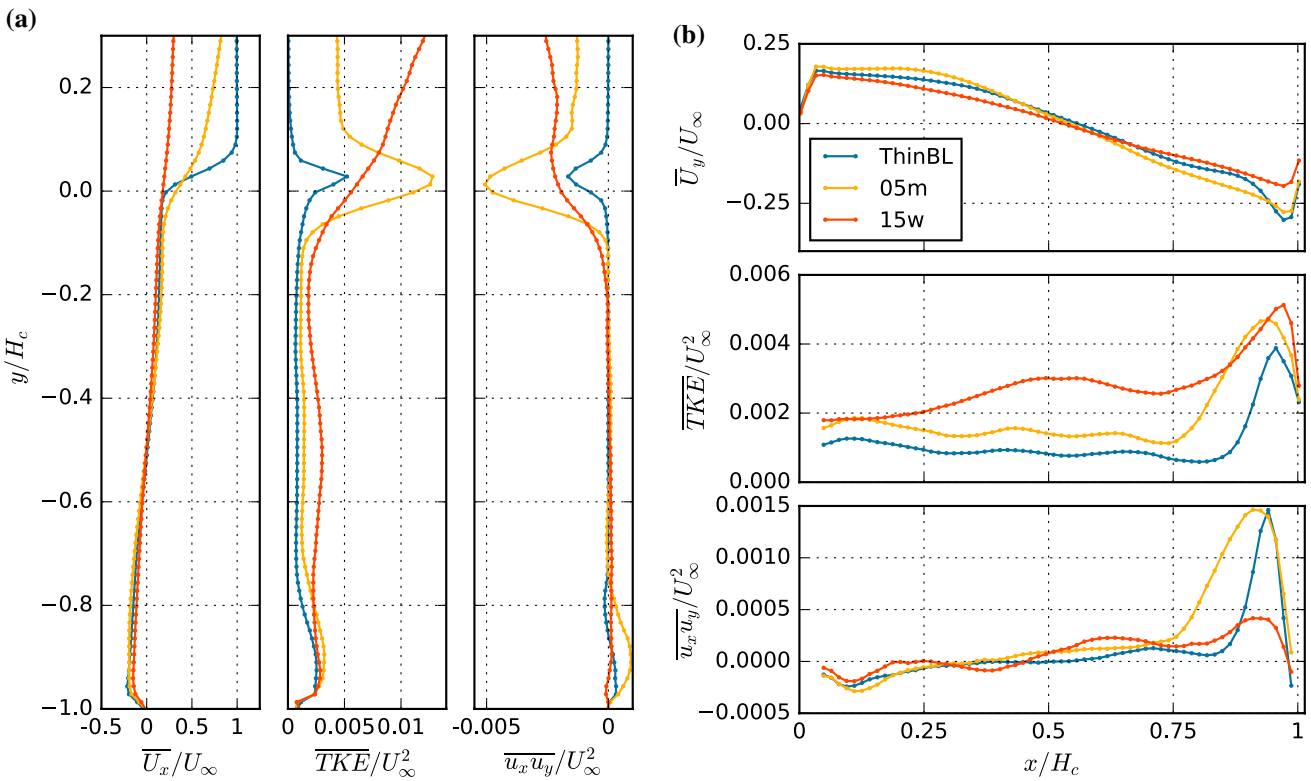

Fig. 5 Profiles of normalized mean velocity, normalized TKE and normalized shear stress $\overline{u_x u_y}$ for the cases *ThinBL*, *5m* and *15w* through the cavity center for **a** a *vertical line* at $x/H_c = 0.5$ and **b** a *horizontal line* at $y/H_c = -0.5$

$\mathcal{P}_{TKE}$, shows a similar picture, with most of the production concentrated in the second half along the cavity top for the case *ThinBL*, but opposite for the case *5m*. The case *15w* shows only weak production at the upstream edge.

Defining a turbulent shear layer through a clearly increased shear stress $-\overline{u_x u_y}$ along the cavity top accompanied by production of normalized TKE, the case *5m* fits that description. Also the case *ThinBL* shows the existence of a shear layer, even if less homogeneous over the full cavity length. For the case *15w*, there is neither a clear increase in normalized shear stress nor an increase in normalized $\mathcal{P}_{TKE}$.

The power spectral density Φ of the horizontal and vertical velocity signal, $U_x(t)$ and $U_y(t)$ has been determined from the time-resolved PIV measurements. The results are shown in Figs. 8 and 9, for the horizontal and vertical velocity respectively, at 5 locations along the cavity top (as indicated in Fig. 7 by the diamonds). Further explanations to the velocity spectra are made in the next section.

The resolved PIV measurements, together with the measured time-averaged flow field, allow to plot spatiotemporal evolution of fluctuating velocity components along a specific line. This has been made for a line along the cavity top for each case and is presented in Fig. 10a, b, for normalized $u_x(t)$ and normalized $u_y(t)$ respectively. From the 5 seconds of acquired data, only the first 1.3 s are shown here.

4 Discussion

This section highlights and discusses some interesting and unique properties of each of the three cavity flows. The cavity flow field statistics, the spectral properties of the shear layer, and the spatiotemporal evolution of the flow have been presented in Sect. 3.

4.1 ThinBL

For the case *ThinBL* only the inlet fetch has been used to generate a boundary layer, without adding turbulence generating spires. The cavity inlet profile (Fig. 3) therefore shows a thin boundary layer and no visible normalized TKE. A further investigation into the shape of the boundary profile (Fig. 11) suggests that the profile is laminar and not turbulent. This is also supported by the Reynolds number $Re_x \approx 165{,}000$ (at a distance $x = 0.86$ m behind the inlet flap) which is below the critical Re_x for a flat boundary layer ($Re_{xcrit} \approx 500{,}000$). The flow inside the cavity however is turbulent, as can be seen from the level of normalized TKE measured by the

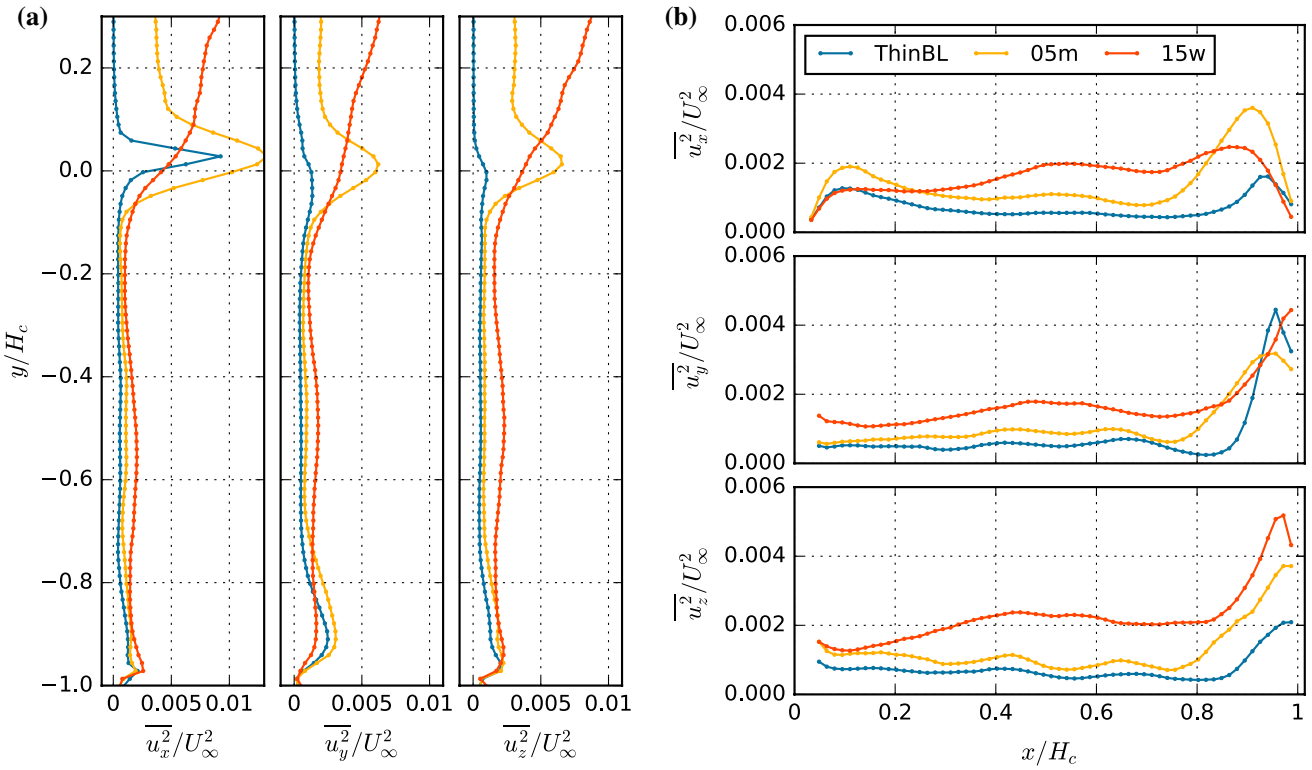

Fig. 6 Profiles of normalized Reynolds stress components $\overline{u_x^2}$, $\overline{u_y^2}$ and $\overline{u_z^2}$ for the cases *ThinBL*, *5m* and *15w* through the cavity center for **a** a *vertical line* at $x/H_c = 0.5$ and **b** a *horizontal line* at $y/H_c = -0.5$

averaged flow statistics (Fig. 5). A particular strong area of normalized TKE and normalized shear stress is observed in the last half of the shear layer (Fig. 7). This coincides with a very large production of normalized TKE. The spectra of horizontal (Fig. 8) and vertical velocity (Fig. 9) reveal clear peaks, with a fundamental frequency and several harmonics. The power spectral density (and also number of harmonics) grows with downstream distance, consistent with the growth of normalized TKE. It should be noted, that the harmonics are magnitudes smaller than the fundamental frequency. The velocity fields (Supplementary Movie 1) show the initial wavelike disturbances to roll-up into large vortices that are mostly two-dimensional with only small, occasional out-of plane velocity. The shear layer, with its distinct vortex shedding, is analyzed in more detail.

With a momentum thickness of $\theta = 1.18$ mm, the ratio of the cavity length to the momentum thickness (L/θ) is 85. This value falls into the range between 80 and 160 where Gharib and Roshko (1987) measured self-sustained shear layer oscillations for a laminar upstream boundary layer. When the vortex shedding is self-oscillating, a mode of $m = 2$ according to the semiempirical model proposed by Rossiter and Britain (1964) is expected (Eq. 3):

$$f = U_c/L(m - \gamma) \tag{3}$$

where f is the fundamental frequency, U_c being the convective velocity and γ an empirical parameter given as 0.25. To get f and U_c from PIV, the equation of a spatially growing wave (Eq. 4) was fitted to the space–time data of vertical velocity at $y/H_c = 0.02$ (Fig. 12b) using a Nelder–Mead donwhill simplex algorithm. 2000 PIV snapshots were used (corresponding to about 100 periods).

$$u_y(x,t) = a + be^{\beta x}\cos(kx - \omega t) \tag{4}$$

From the fitted wavenumber k and angular frequency ω, the frequency is calculated as $f = \omega/(2\pi)$ and the convective velocity as $U_c = \omega/k$. This method of simultaneously extracting the frequency and the wavelength has proved to be far more robust than a combination of spectral analysis for the frequency and lagged two-point auto-correlation for the convective velocity. The result from the fitting are $U_c = 1.78$ m/s and $f = 31.5$ Hz. Together with Eq. 4, the cavity oscillation mode results in $m = 2.04$, relating the shear layer vortex shedding to self-sustained oscillations.

In addition to the fundamental frequency, the shear layer also exhibits low frequency disturbances. These disturbances are clearly visible in Fig. 10a as large areas of increased or decreased in horizontal velocity. Since the space–time representation of the horizontal velocity fluctuations is highly sensitive to a vertical displacement, we

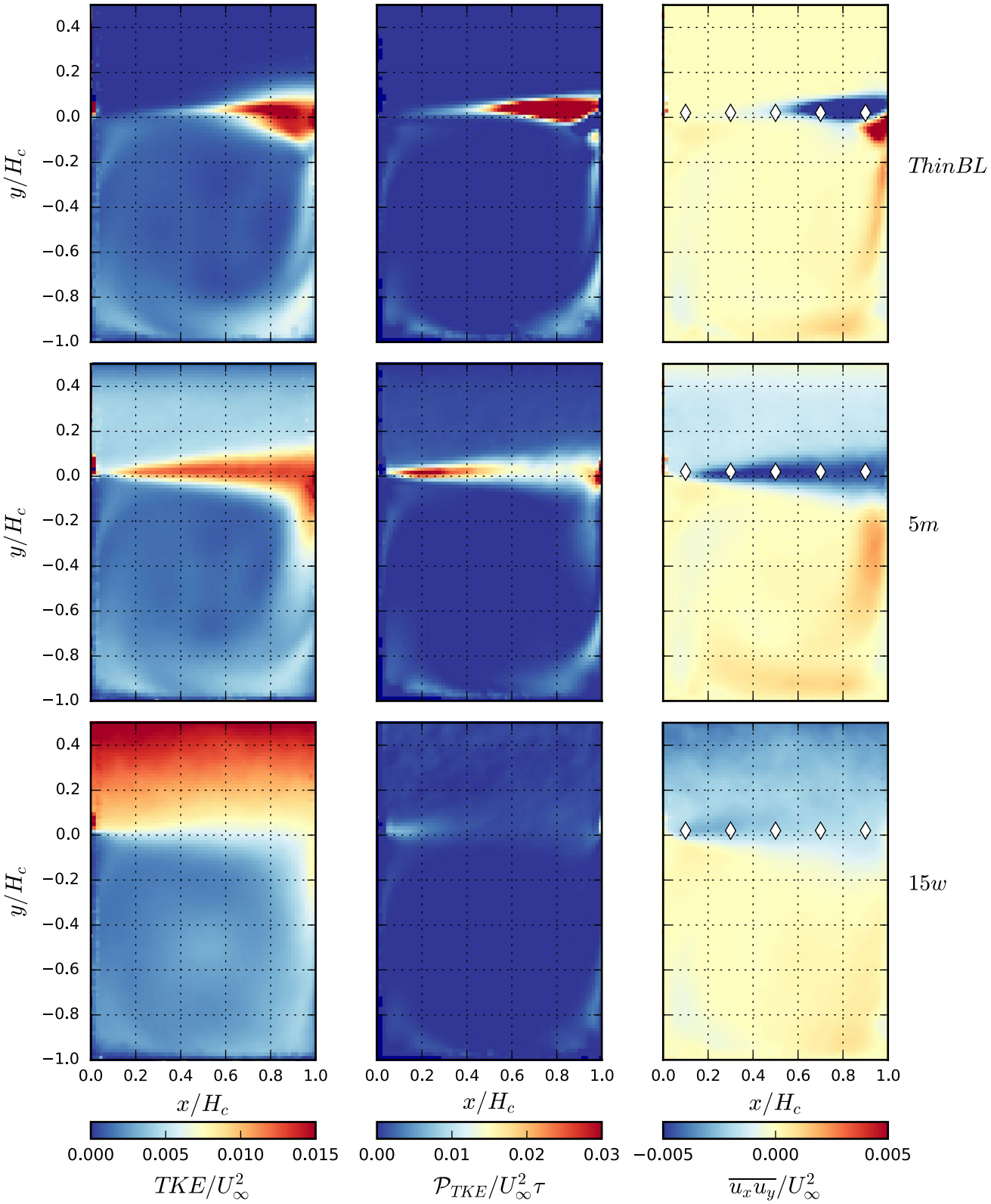

Fig. 7 Normalized turbulent kinetic energy (TKE), production of normalized TKE and normalized shear stress for the three cases *ThinBL* (*top*), *5m* (*middle*) and *15w* (*bottom*). *White diamond markers* show the location of point probes used for spectral analysis

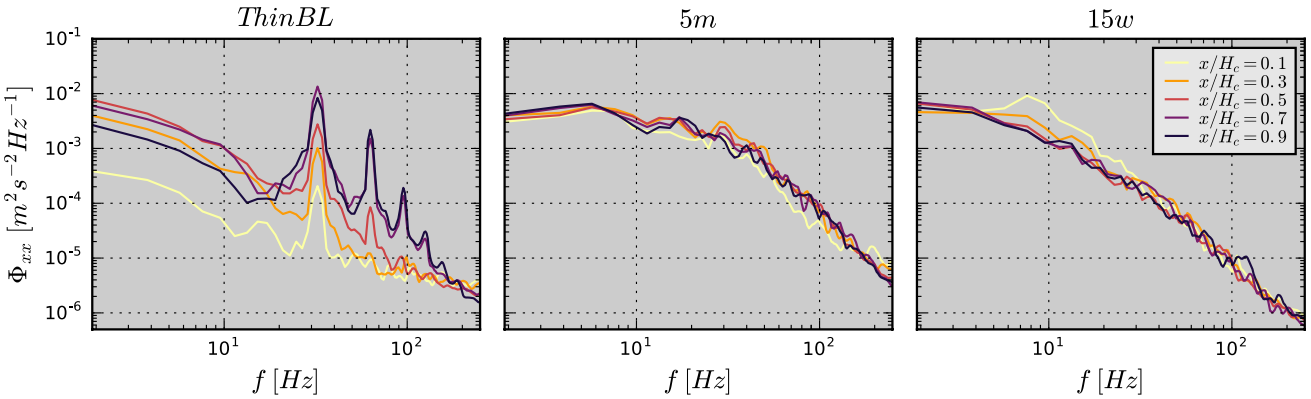

Fig. 8 Power spectral density of the horizontal (streamwise) velocity component U_x for three cases *ThinBL* (*left*), *5m* (*middle*) and *15w* (*right*), evaluated at different horizontal locations along the cavity top

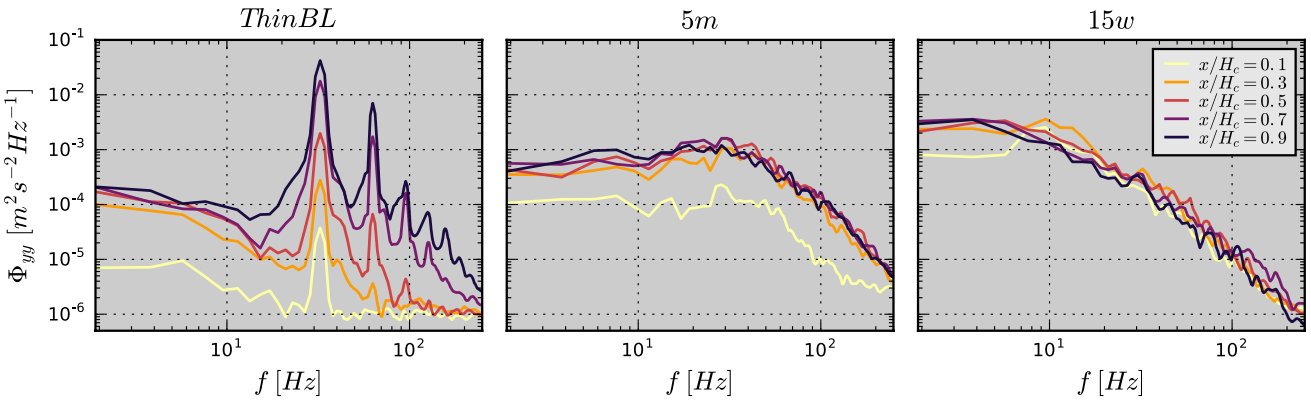

Fig. 9 Power spectral density of the vertical velocity component U_y for three cases *ThinBL* (*left*), *5m* (*middle*) and *15w* (*right*), evaluated at different horizontal locations along the cavity top

assume this is due to a low frequency flapping. To assess that this is not caused by external disturbances, horizontal space–time plots at different heights are extracted (Fig. 12). At $y/H_c = 0.08$ above the cavity top, no disturbances can be observed upstream of the cavity, indicating that these disturbances are not present in the approach flow. When comparing the vertical fluctuations at $y/H_c = -0.04$ and the horizontal fluctuations at $y/H_c = 0.02$, a correlation can be observed, consistent with a low frequency flapping. This low frequency flapping of the shear layer has been observed in previous measurements and was studied in detail by Basley et al. (2013) and Liu and Katz (2013).

4.2 5m

By placing 5-cm-tall spires ($H_s = 0.5H_c$) upstream of the cavity, a turbulent boundary layer is generated with a moderate level of turbulence intensity (2 %) and a momentum thickness of $\theta = 7.76$ mm. The cavity is located sufficiently far downstream of the spires, that the geometrical pattern of the spires is not visible in the average flow field (Fig. 2). The boundary layer is therefore composed of a decaying spire wake flow and a growing internal boundary layer generated by the inlet fetch. The flow profile is close to a power law profile (Fig. 13). Together with the TKE and shear stress profiles reported in Fig. 3, the experimental setup is therefore capable of simulating a turbulent boundary layer.

The analysis of the average flow field shows a clear increase in normalized TKE in the shear layer (Fig. 7), and the thickness increases linearly with downstream distance. The production of normalized TKE is concentrated in the first half of the shear layer, with a maximum at $x/H_c = 0.2$. To elucidate this peak, the contribution of each term in the TKE production equation (Eq. 2) is compared. The term $\overline{u_x u_y}\ \frac{\partial u_x}{\partial y}$ is found to be dominant, and is shown in Fig. 14. The high velocity gradient at the beginning of the shear layer and the rising normalized shear stress culminate to a peak and then fall to an almost constant level up to where the downstream cavity edge becomes influential.

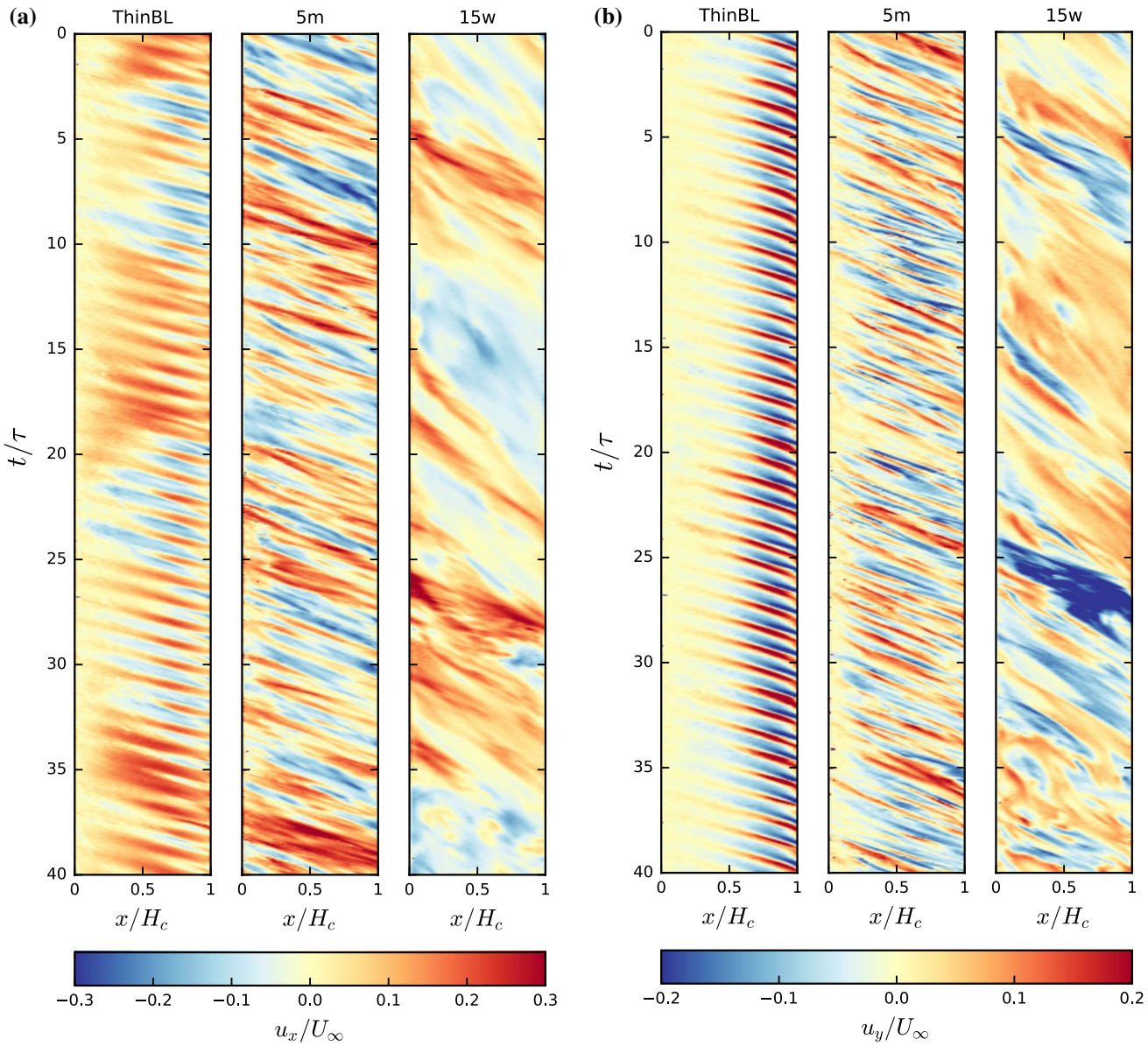

Fig. 10 Space–time plots of fluctuating normalized velocity u_x (**a**) and normalized u_y (**b**) in the shear layer at $y/H_c = 0.02$

The characteristics are similar to what can be found for a backward-facing step (Kostas et al. 2002). The shear layer velocity spectra (shown in Figs. 8 and 9) show an increase in power spectral density Φ with increasing distance, most notably for the vertical velocity between $x/H_c = 0.1$ and $x/H_c = 0.3$ and less pronounced up to $x/H_c = 0.7$. Compared to the case *ThinBL*, no clear peak that would correspond to a fundamental frequency is visible. To show the growth in spectral power, noise removal had to be applied by using Welch's Method (Welch 1967) when generating the spectra. This however also removes sharp peaks. For single point spectra with no smoothing, it is difficult to distinguish peaks from noise, therefore a spatial spectrogram was computed. From the spatial persistence, it's possible to identify spectral peaks that originate from shear layer flow structures. Figure 15 shows clearly that characteristic frequencies exist. The largest peak is observed at 30.81 Hz. The associated Φ grows until the position reaches about $0.8\,x/H_c$ downstream. After that, the peak at 29.1 Hz becomes dominant. It appears, that the turbulent kinetic energy is transferred between the frequencies. This could be due to a vortex pairing and breakup, and/or interaction with boundary layer coherent structures.

An example of such complex vortex interaction, pairing and breakup is shown in the snapshots in Fig. 16 or in Supplementary Movie 2. In addition, Fig. 16 visualizes the

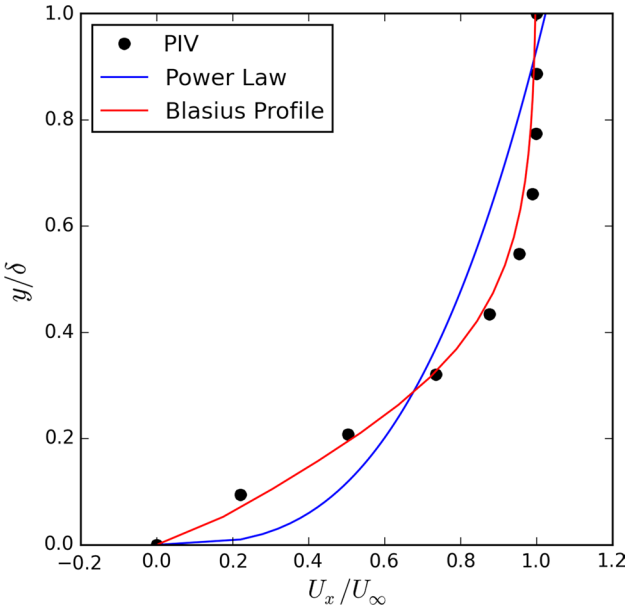

Fig. 11 Inlet profile of case *ThinBL* in comparison with the Blasius solution for a laminar boundary layer and the power law of a turbulent boundary layer, normalized by the boundary layer thickness and the free stream velocity

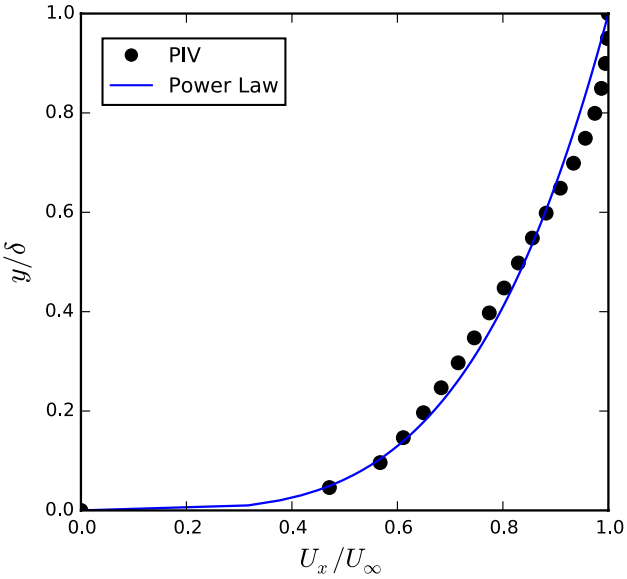

Fig. 13 Inlet profile of case *5m* compared to a fit with a power law, normalized by the boundary layer thickness and the free stream velocity

out-of-plane normalized velocity component u_z, showing that the vortices in the shear layer, other than in the case *ThinBL*, are not predominantly two-dimensional, but interact with the three-dimensional structures of the boundary layer. Besides the constant shedding of new coherent structures in the shear layer, and their interaction with each other and the external flow, no other repeating pattern can be observed when looking at more snapshots. This lack of a single dominant periodicity can also be seen in the space–time plots (Fig. 10).

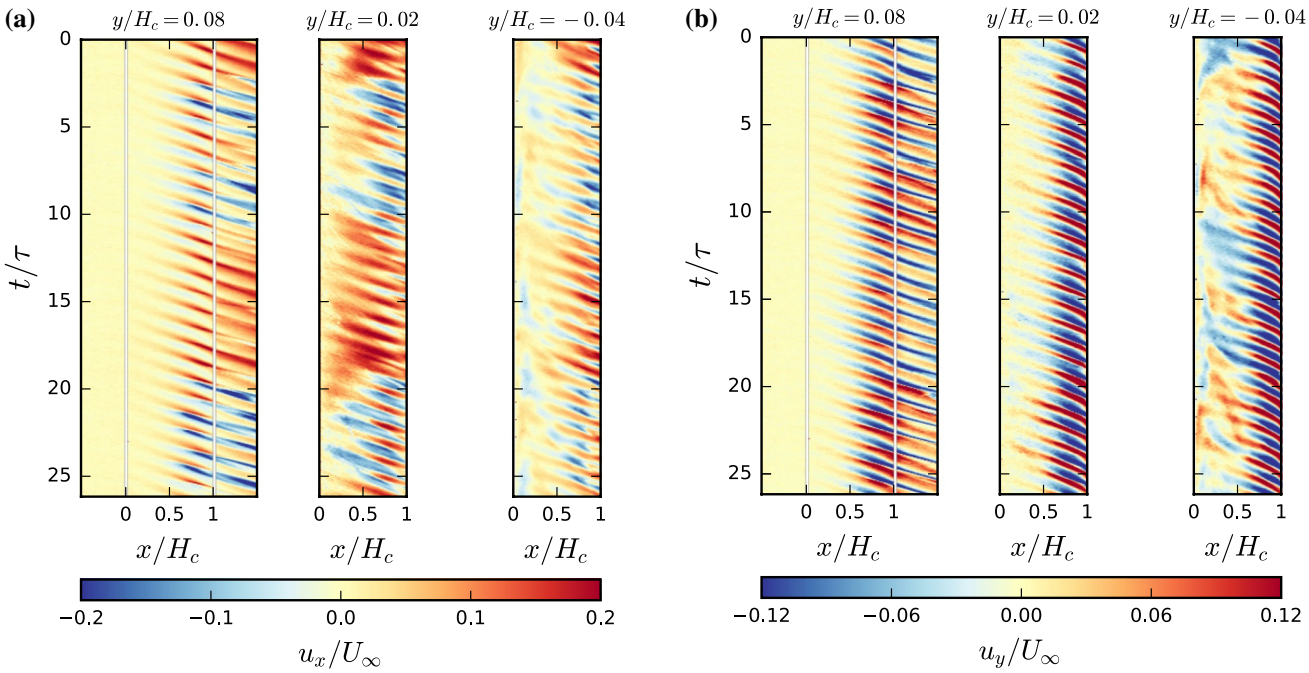

Fig. 12 Space–time plots of fluctuating velocity u_x (**a**) and u_y (**b**) in the shear layer at three locations ($y/H_c = 0.08$, $y/H_c = 0.02$, $y/H_c = -0.04$) for the case *ThinBL*

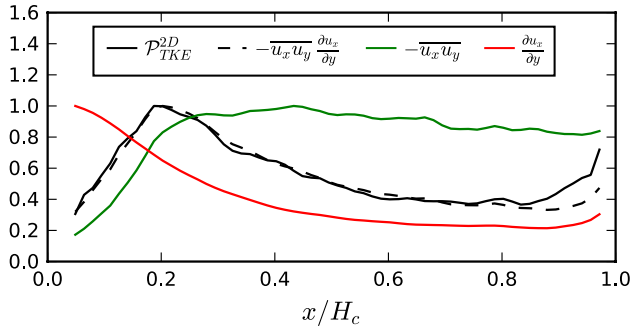

Fig. 14 Spatial evolution of $\mathcal{P}_{TKE}$ along the cavity top ($y/H_c = 0.02$), together with the dominant term and its components. Each value is normalized by its maximum

The momentum thickness was determined by integrating the boundary layer profile. With a momentum thickness of $\theta = 7.76$ mm the ratio L/θ is equal to 13. This is well below the range where self-sustained oscillations are expected to occur. This, together with the absence of a clear fundamental frequency, means possibly that the main mechanism for vortex formation is the natural Kelvin–Helmholtz instability of the shear layer, but disturbed by the turbulent structures of the external flow.

4.3 15w

The third case features a turbulent upstream wake flow with 15 % turbulence intensity, generated by 15-cm-tall spires ($H_s = 1.5H_c$), with a width of 4.6 cm at the base. The hot wire measurements (Fig. 2) show a large wake behind the spires. The horizontal plane measured suggests, that the spire wakes of multiple neighboring spires join together to form a larger wake. This is presumably due to the large blockage (≈30 %) of the spires, making them act in parts like a barrier where flow is pushed over the top and not predominantly act like turbulence generators.

The location of the cavity is downstream of the main wake zone of the spires. With the spire wake reattachment length x_r measuring around 0.3m, this places the cavity roughly twice x_r downstream. This results in a cavity inlet flow with distinctive events of large disturbance. This can be seen especially well in Fig. 10b, where large events of negative vertical velocity are observed, for example at $t/\tau = 26$.

If we consider an event to be a bulk motion of fluid into or out of the cavity, a high momentum but infrequent event would not appear in, e.g., the autocorrelation function (used to determine the integral time scale), or the spectral

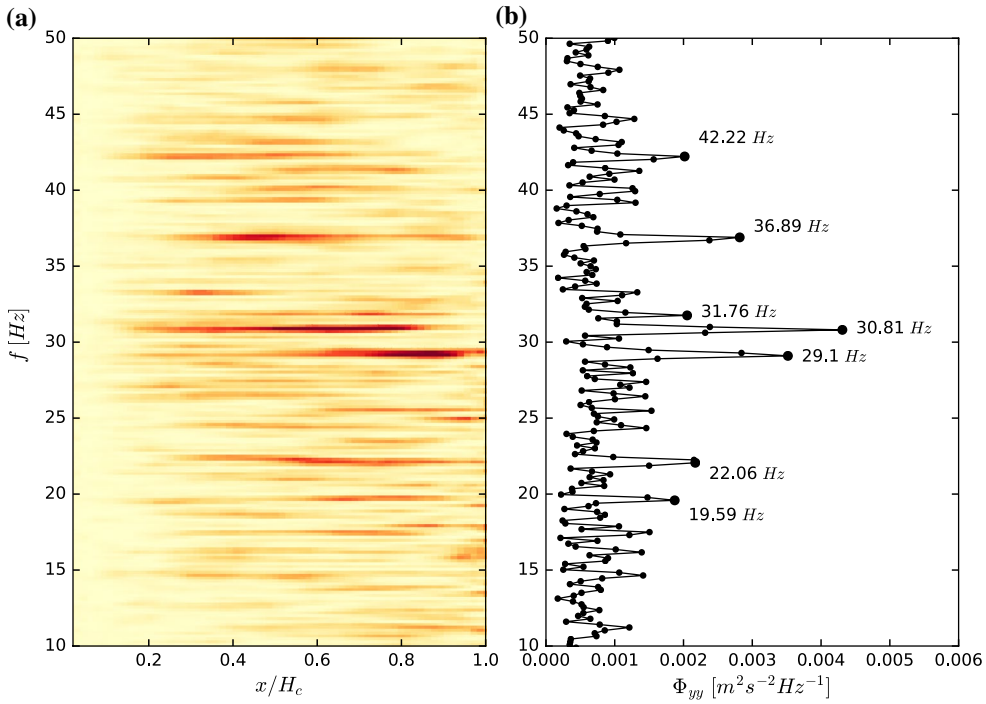

Fig. 15 Shear layer power spectral density Φ of u_y for the case *5m* showing **a** the spatial evolution in the shear layer and **b** the magnitude of the spatial average

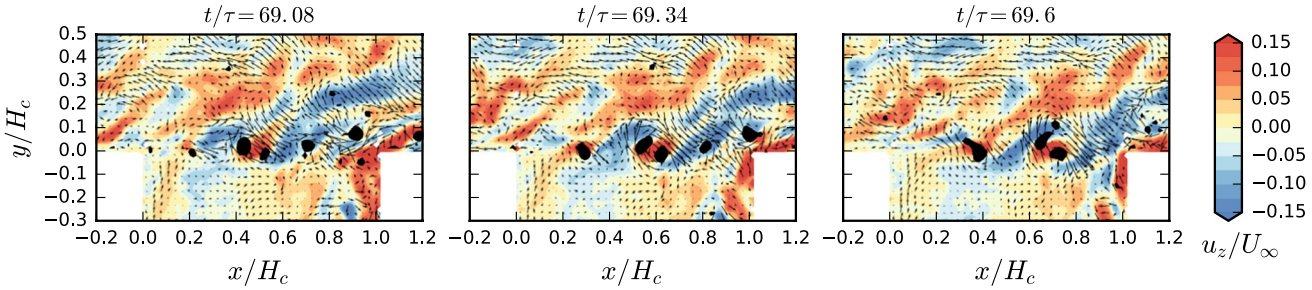

Fig. 16 Sequential snapshots of the case *5m*, showing instantaneous fluctuation velocity (vectors), normalized out-of-plane velocity u_z (*color*) and vortex cores obtained from Q^{2D} (*black*)

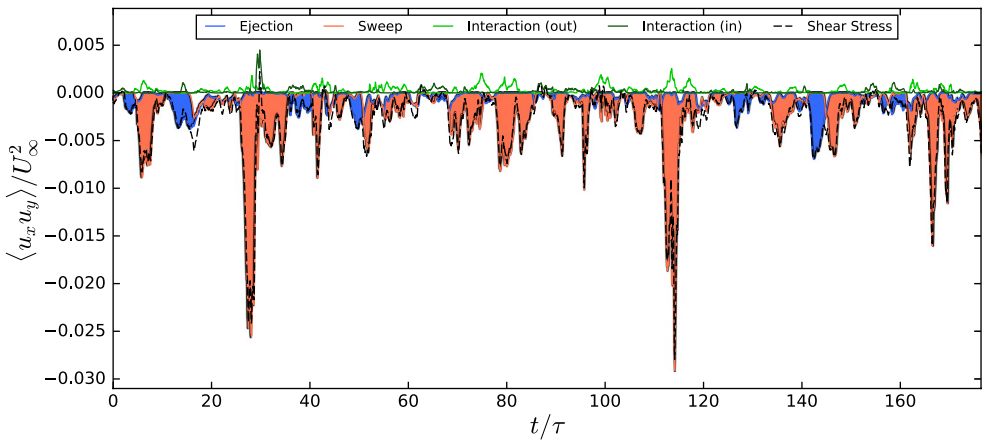

Fig. 17 Temporal evolution of the spatially averaged normalized shear stress $\overline{u_x u_y}$ along the cavity top at $y/H_c = 0.02$. *Colored lines* show the contribution of the 4 quadrants, and the *colored ares* show the difference in magnitude of sweep and ejection

analysis shown in Figs. 8 and 9. In order to find and classify events, the quadrant method has been applied. However, instead of using uncorrelated PIV snapshots to compute the histogram of the four quadrants, the normalized shear stress $\overline{u_x u_y}$ was computed from spatiotemporal velocity fluctuations (Fig. 10), spatially averaged over the cavity top and subsequently decomposed into the four quadrants. The resulting time evolution is shown in Fig. 17 and in Supplementary Movie 3.

It is immediately apparent, that sweep events dominate the shear layer. Within this measurement period, two very strong sweep events are detected, around $t/\tau = 27$ and $t/\tau = 115$. Ejection events also occur, and are similar in magnitude as the smaller, more numerous sweep events. Further insights into these events can be gained by plotting the spatiotemporal evolution of sweep/ejections overlaid with the vortex criteria Q in the shear layer. In the left panel in Fig. 18, we observe that Q is usually associated with sweep. The slope of structures relates to the velocity at which these structures are convected through the shear layer. We look at four events (as defined in Fig. 18). The sweep event A and D show a higher U_c than event C. The two events A and B seem to be associated with large-scale, high velocity vortical structures in the wake flow, presumably generated by the interaction of the spire wake with the high velocity free stream flow. Event C in contrast features smaller structures, resembling more the structures of a turbulent boundary layer. While the sweep in event A and C is mostly convected over the cavity, event D shows a penetration of high momentum fluid into the cavity. This area of high momentum also contains numerous small coherent structures, that are transported into the cavity. Additionally, new vortical structures form at the interface of the sweep and the low momentum cavity fluid.

A distinct mechanism of vortex formation can be observed for all sweep events (A, C and D): high momentum fluid passes over the upstream corner of the cavity, separates at the edge and due to the high velocity gradient sheds a vortex with the axis parallel to the cavity edge. This is supported by the correlation of a sweep at the leading edge, and the subsequently detected vortex (left panel in Fig. 18). This vortex shedding mechanism shows up as a production of TKE, as visible in Fig. 7. It is believed, that this is also responsible for the peaks in the power spectral density at $x/H_c = 0.1$ and $x/H_c = 0.3$ (Figs. 8 and 9).

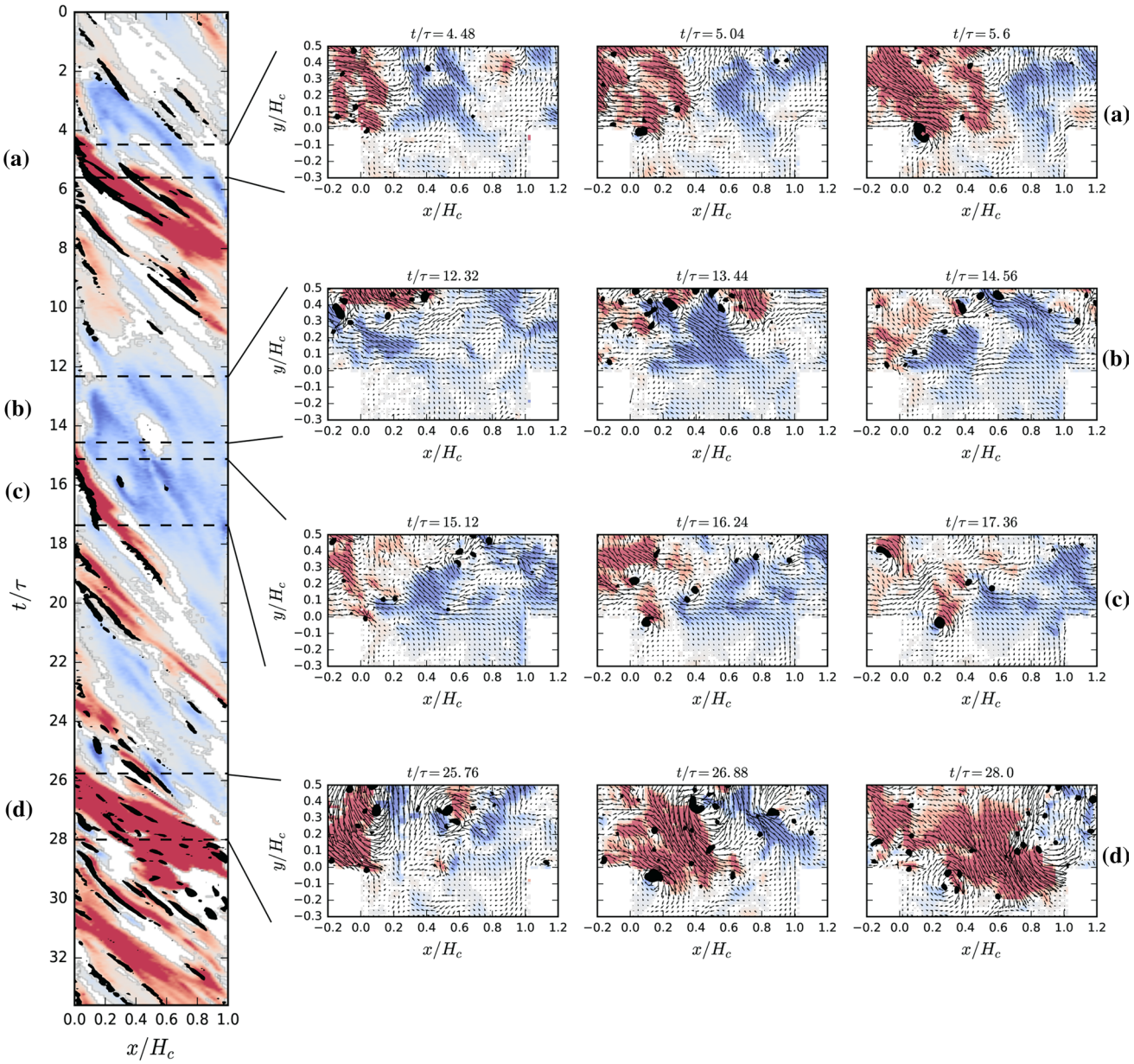

Fig. 18 Space–time representation (*left*) and snapshots (*right*) of sweep (*red*) and ejection (*blue*) events in the shear layer at $y/H_c = 0.02$, overlaid by the vortex cores obtained from Q^{2D} (*black*). Vectors are instantaneous fluctuation velocity. The snapshots represent four selected events, *from top to bottom* sweep (**a**), ejection (**b**), sweep (**c**), sweep (**d**)

The observed, distinct events of flow entrainment (sweeps) and flushing (ejections), pose difficulties for RANS modellers since these flows are not predominantly described by classical shear layer statistics. Time-resolved PIV in combination with scalar transport, such as PIV–LIF (light induced fluorescence) or quantitative light sheet (QLS) enables to perform flushing events measurements and compute ensemble averages. The main challenge for time-resolved numerical simulations (e.g., large eddy simulation) is to efficiently provide highly turbulent and intermittent inflow conditions, such as generated in these measurements.

5 Summary

Time-resolved and time-averaged stereo-PIV measurements have been performed on a 2D unit aspect ratio shear-driven cavity. Cavity flow experiments are usually conducted for a specific type of inflow condition. In our

experiment, a split-floor design was used in combination with or without turbulence generating spires to successfully generate different inflow boundary layers, from laminar to highly turbulent, developed and developing.

The experimental setup was capable of producing two typical cavity flows. The case with the thin boundary layer shows the expected self-sustained oscillations at a distinct frequency. A thicker, more turbulent boundary layer shows classical shear layer growth and vortex shedding through Kelvin–Helmholtz type instabilities. Even tough self-sustained oscillations can occur when the upstream boundary layer is turbulent and thicker, our measurements showed no clear indications that resonance phenomena are present. The third case features highly turbulent and intermittent inflow conditions, for which no comparable measurements exist in current literature. The case can be interpreted as a street canyon located in the wake of a larger upstream obstacle (building or topography). Instead of vortex formation in the shear layer, as observed with the moderately turbulent inflow, vortex shedding can be observed at the upstream corner, due to upstream edge flow detachment caused by strong sweep events. The main observations made from the three specific flows are summarized as follows:

- The mean flow topology (streamlines) is similar for each case, showing a large main vortex, two corner vortices at the floor and a vortex at the upstream corner. This suggests that for this experiment the cavity geometry (aspect ratio) determines the vortex pattern.
- A clear shear layer spanning the cavity top, defined through shear stress and production of TKE, was observed when the upstream boundary layer was laminar or moderately turbulent. With strong turbulence, no clear shear layer TKE production was visible.
- Coherent structures at the cavity top are produced in each case, however the production location and mechanism is significantly different (self-sustained oscillations versus Kelvin–Helmholtz vortices versus upstream edge vortex shedding).
- Not only relying on statistical analysis based on mean flow quantities and spectral analysis, revealed transient events such as the strong sweep events observed for the case *15w*.

Even though the investigated turbulent boundary layer and turbulent wake flow are quite specific, the measurements have shown the differences of the shear layer when large-scale turbulence and disturbances exist in the upstream flow. It is therefore expected, that the exchange of scalars such as pollutant and heat in and out of the cavity is governed significantly by these large-scale events, instead of the shear layer dynamics. This is posing unique problems for RANS and LES modellers.

Acknowledgments This work was supported by the Hartmann Müller-Fonds on Grant ETH-32 11-2.

References

Ashcroft G, Zhang X (2005) Vortical structures over rectangular cavities at low speed. Phys Fluids 17(1):015104. doi:10.1063/1.1833412

Basley J, Pastur LR, Lusseyran F, Faure TM, Delprat N (2010) Experimental investigation of global structures in an incompressible cavity flow using time-resolved PIV. Exp Fluids 50(4):905–918. doi:10.1007/s00348-010-0942-9

Basley J, Pastur LR, Delprat N, Lusseyran F (2013) Space-time aspects of a three-dimensional multi-modulated open cavity flow. Phys Fluids 25(6):064105. doi:10.1063/1.4811692

Bian S, Driscoll JF, Elbing BR, Ceccio SL (2010) Time resolved flowfield measurements of a turbulent mixing layer over a rectangular cavity. Exp Fluids 51(1):51–63. doi:10.1007/s00348-010-1025-7

Chang K, Constantinescu G, Park SO (2006) Analysis of the flow and mass transfer processes for the incompressible flow past an open cavity with a laminar and a fully turbulent incoming boundary layer. J Fluid Mech 561:113. doi:10.1017/S0022112006000735

Chatellier L, Laumonier J, Gervais Y (2004) Theoretical and experimental investigations of low Mach number turbulent cavity flows. Exp Fluids 36(5):728–740. doi:10.1007/s00348-003-0752-4

Gharib M, Roshko A (1987) The effect of flow oscillations on cavity drag. J Fluid Mech 177(1):501. doi:10.1017/S002211208700106X

Haigermoser C, Vesely L, Novara M, Onorato M (2008) A time-resolved particle image velocimetry investigation of a cavity flow with a thick incoming turbulent boundary layer. Phys Fluids 20(10):105101. doi:10.1063/1.2990043

Hunt J, Wray A, Moin P (1988) Eddies, streams, and convergence zones in turbulent flows. In: Studying turbulence using numerical simulation databases, 2 proceedings of the 1988 summer program, pp 193–208. http://adsabs.harvard.edu/abs/1988stun.proc..193H%EF%BF%BD%C3%9C

Hussain M, Lee B (1980) An investigation of wind forces on three-dimensional roughness elements in a simulated atmospheric boundary layer flow Part 2. Flow over large arrays of identical roughness elements and the effect of frontal and side ratio variations. Technical report, Dept of Building Science, University of Sheffield, Report BS 56

Immer M (2015) Cavity flow PIV dataset. http://www.carmeliet.arch.ethz.ch/ResearchDatabase/CavityFlow. Accessed 10 Sept 2015

Irwin H (1981) The design of spires for wind simulation. J Wind Eng Ind Aerodyn 7(3):361–366. doi:10.1016/0167-6105(81)90058-1

ITTC (2008) ITTC recommended procedures and guidelines—uncertainty analysis particle imaging velocimetry. Technical report

Johnson W, Ludwig F, Dabberdt W, Allen R (1973) An urban diffusion simulation model for carbon monoxide. J Air Pollut Control Assoc 23(6):490–498. doi:10.1080/00022470.1973.10469794

Kang W, Sung HJ (2009) Large-scale structures of turbulent flows over an open cavity. J Fluids Struct 25(8):1318–1333. doi:10.1016/j.jfluidstructs.2009.06.005

Kang W, Lee SB, Sung HJ (2008) Self-sustained oscillations of turbulent flows over an open cavity. Exp Fluids 45(4):693–702. doi:10.1007/s00348-008-0510-8

Kellnerová R, Kukačka L, Jurčáková K, Uruba V, Jaour Z (2012) PIV measurement of turbulent flow within a street canyon: detection of coherent motion. J Wind Eng Ind Aerodyn 104–106:302–313. doi:10.1016/j.jweia.2012.02.017

Knisely C, Rockwell D (1982) Self-sustained low-frequency components in an impinging shear layer. J Fluid Mech 116(1):157. doi:10.1017/S002211208200041X

Kostas J, Soria J, Chong M (2002) Particle image velocimetry measurements of a backward-facing step flow. Exp Fluids 33(6):838–853. doi:10.1007/s00348-002-0521-9

LaVision (2011a) DaVis 8.0 Software Manual. LaVision GmbH

LaVision (2011b) FlowMaster Manual. LaVision GmbH

Liu X, Katz J (2013) Vortex-corner interactions in a cavity shear layer elucidated by time-resolved measurements of the pressure field. J Fluid Mech 728:417–457. doi:10.1017/jfm.2013.275

Nicholson SE (1975) A pollution model for street-level air. Atmos Environ 9(1):19–31. doi:10.1016/0004-6981(75)90051-7

Nobach H, Tropea C (2007) Fundamentals of data processing. In: Tropea C, Yarin A, Foss J (eds) Springer handbook of experimental fluid mechanics. Springer, Berlin, pp 1399–1417. doi:10.1007/978-3-540-30299-5_23

Nunez M, Oke TR (1977) The energy balance of an urban canyon. J Appl Meteorol 16(1):11–19. doi:10.1175/1520-0450(1977)016<0011:TEBOAU>2.0.CO;2

Oke T (1988) Street design and urban canopy layer climate. Energy Build 11(1–3):103–113. doi:10.1016/0378-7788(88)90026-6

Rockwell D (1977) Prediction of oscillation frequencies for unstable flow past cavities. J Fluids Eng 99(2):294. doi:10.1115/1.3448746

Rockwell D, Naudascher E (1978) Review–self-sustaining oscillations of flow past cavities. J Fluids Eng 100:14. doi:10.1115/1.3448624

Roshko A (1955) Some measurements of flow in a rectangular cutout. Technical Report August 1955. http://oai.dtic.mil/oai/oai?verb=getRecord&metadataPrefix=html&identifier=ADA377172

Rossiter J, Britain G (1964) Wind-tunnel experiments on the flow over rectangular cavities at subsonic and transonic speeds. Technical report. http://repository.tudelft.nl/view/aereports/uuid:a38f3704-18d9-4ac8-a204-14ae03d84d8c/

Salizzoni P, Marro M, Soulhac L, Grosjean N, Perkins RJ (2011) Turbulent transfer between street canyons and the overlying atmospheric boundary layer. Bound Layer Meteorol 141(3):393–414. doi:10.1007/s10546-011-9641-1

Sarohia V (1975) Experimental and analytical investigation of oscillations in flows over cavities. PhD thesis. http://thesis.library.caltech.edu/1597/

Welch P (1967) The use of fast Fourier transform for the estimation of power spectra: a method based on time averaging over short, modified periodograms. IEEE Trans Audio Electroacoust 15(2):70–73. doi:10.1109/TAU.1967.1161901

Wieneke B (2005) Stereo-PIV using self-calibration on particle images. Exp Fluids 39(2):267–280. doi:10.1007/s00348-005-0962-z

Wieneke B (2014) Generic a-posteriori uncertainty quantification for PIV vector fields by correlation statistics. ltcesdemistutlpt pp 7–10. http://ltces.dem.ist.utl.pt/lxlaser/lxlaser2014/finalworks2014/papers/03.5_2_560paper.pdf